14 Quantum Criticality and Superconductivity in Diagrammatic Extensions of DMFT

Karsten Held
Institute of Solid State Physics, TU Wien
1040 Vienna, Austria

Contents

E. Pavarini, E. Koch, A. Lichtenstein, and D. Vollhardt (eds.)
DMFT: From Infinite Dimensions to Real Materials
Modeling and Simulation Vol. 8
Forschungszentrum Jülich, 2018, ISBN 978-3-95806-313-6
http://www.cond-mat.de/events/correl18

1 Introduction

Dynamical mean field theory (DMFT) [1, 2] has been a breakthrough for describing electronic correlations in models [3] and – in combination with density functional theory – even in actual materials [4–6]. This breakthrough has been brought about since DMFT includes a major part of the electronic correlations, namely the local ones. On the other hand, the arguably most fascinating physical phenomena such as (quantum) criticality, high-temperature superconductivity and vertex corrections to the conductivity rely on non-local correlations.

Hence, in recent years these non-local correlations have been at the focus of the methodological development. There are two routes that include the local DMFT correlations but also incorporate non-local correlations beyond. On the one hand there are cluster extensions of DMFT, which take instead of the single site of DMFT a cluster of lattice sites that is embedded in a dynamical mean field. This way correlations within the cluster are taken into account. For a review see [7] and for a pedagogical introduction see the lecture by Th. Maier in this School.

Because of numerical limitations the size of the cluster is, however, limited to about 10×10 lattice sites and even less in the case of realistic multi-orbital calculations. This is sufficient to describe short range correlations; and indeed cluster extensions of DMFT have been highly successful for describing pseudogaps and d-wave superconductivity in the two-dimensional ($2d$) Hubbard model. However long-range correlations as they occur for example in the vicinity of a phase transition cannot be described in this way.

For including short- and long-range correlations on an equal footing, in recent years, diagrammatic extensions of DMFT have been developed. This development started with the dynamical vertex approximation (DΓA) [8] and the dual fermion (DF) approach [9], continuing with a plethora of further approaches [10–13]. All of these approaches take a local two-particle vertex as a starting point and from this construct the local DMFT correlations as well as non-local correlations beyond. The difference lies in the details: which vertex is taken, by which Green functions these are connected, and which Feynman diagrams are considered. For a review, see [14]. Successes of these diagrammatic extensions of DMFT include the calculation of critical exponents in the Hubbard [15,16] and Falicov-Kimball model [17], quantum criticality in the $3d$ Hubbard [18] and $2d$ periodic Anderson model [19], the suppression of antiferromagnetism by spin fluctuations in the $3d$ and $2d$ Hubbard model [20, 15, 21], the fate of the Mott-Hubbard metal-insulator transition for the $2d$ Hubbard model [22], pseudogaps [23, 20, 11, 24, 25, 12] and superconductivity [21, 26] in the $2d$ Hubbard model.

In the following we first give a brief synopsis of the DΓA approach in Section 2, for further reading see the Lecture Notes [27] and the review [14]. For an introduction to the DF approach we refer the reader to the Chapter by H. Hafermann in these Lecture Notes, as well as to [14]. The main focus of the present Lectures Notes is on physical results, starting with the critical and quantum critical properties of the $3d$ Hubbard model in Section 3 and 4, respectively. The quantum critical properties of the $2d$ periodic Anderson model are discussed in Section 5, before we turn to superconductivity in the $2d$ Hubbard model in Section 6. Finally, Section 7 provides a brief summary and outlook.

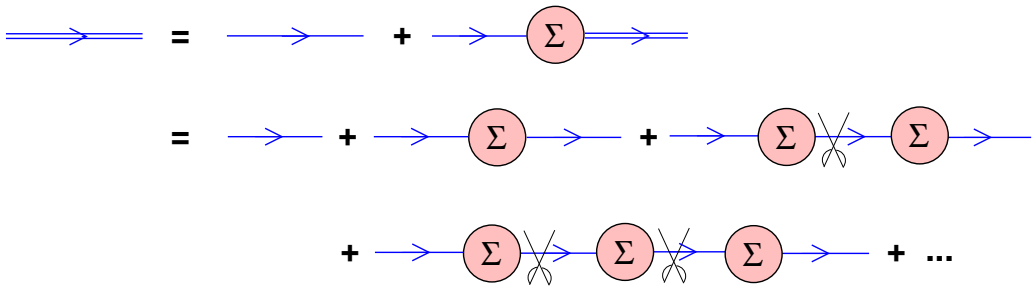

Fig. 1: *Dyson equation connecting Green function and self energy. The pair of scissors indicates that these diagrams are one-particle reducible (i.e., cutting one G_0 line separates the Feynman diagram into two parts). From [27].*

2 Synopsis: Dynamical vertex approximation

The basic idea of the dynamical vertex approximation (DΓA) is a resummation of Feynman diagrams, not in order-by-order of the Coulomb interaction as in conventional perturbation theory, but in terms of their locality. That is, we assume the fully irreducible n-particle vertex to be local and from this building block we construct further diagrams and non-local correlations. The first level ($n = 1$) is then just the DMFT which corresponds to all local Feynman diagrams for the self-energy Σ. Note that Σ is nothing but the fully irreducible $n = 1$-particle vertex. One particle-irreducibility here means that cutting one Green function line does not separate the Feynman diagram into two pieces. Indeed, such reducible diagrams must not be included in the self-energy since it is exactly these diagrams that are generated from the Dyson equation which resolved for G reads

$$G_{\nu\mathbf{k}} = \left(1/G_{0,\nu\mathbf{k}} - \Sigma_{\nu\mathbf{k}}\right)^{-1} \tag{1}$$

for momentum $\mathbf{k}$, Matsubara frequency ν and non-interacting Green function $G_{0,\nu\mathbf{k}}$. For an illustration, see Fig. 1, which also explicitly shows how one-particle reducible diagrams are generated through the Dyson equation; and hence must not be contained in the Σ-diagrams
On the next level, for $n=2$, we assume the locality of the two-particle fully irreducible vertex Λ. That is cutting two Green function lines does not separate the diagram into two pieces. There is a set of exact equations, coined parquet equations [28–30, 14], that allows us to calculate from a given Λ the full vertex, self-energy, and Green function as well as the irreducible vertices Γ_ℓ in three different channels ℓ.
For understanding how these irreducible vertices Γ_ℓ and Λ come about, we consider in Fig. 2 the parquet decomposition of the full vertex F into the fully irreducible vertex Λ and those parts that are two-particle reducible. There are three distinct such reducible parts Φ_ℓ, since say leg 1 may stay connected with leg 2, 3, or 4 when cutting two Green function lines as indicated in Fig. 2. The irreducible vertex is just the complement: $\Gamma_\ell = F - \Phi_\ell$. The three possible channels ℓ are denoted as particle-hole (ph), transversal particle-hole ($\overline{ph}$) and particle-particle (pp) channel. It is important to note that each reducible diagram is contained in one and only one of these channels.[1]

[1] One can easily show that otherwise cutting lines would result in a diagram with one incoming and two outgoing lines, which is not possible because of the conservation of (fermionic) particles.

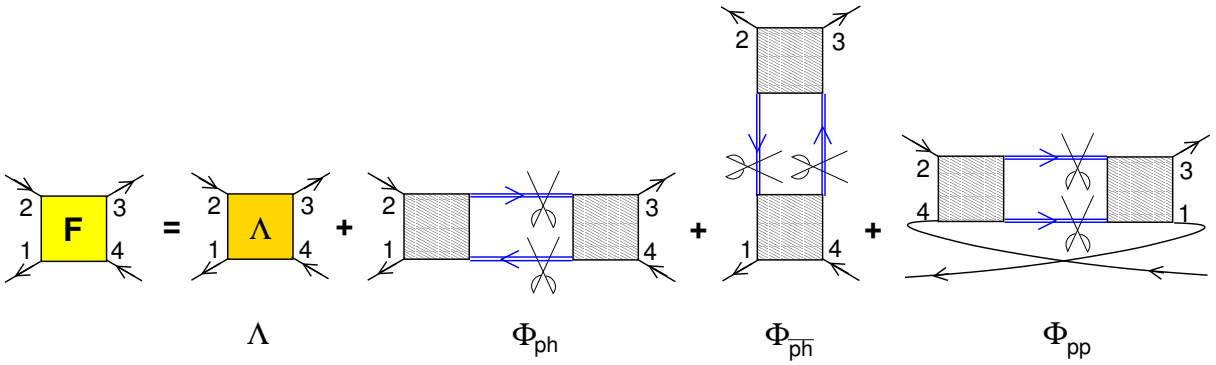

Fig. 2: *Parquet decomposition of the full (reducible) vertex F into the fully irreducible vertex Λ and two-particle reducible diagrams Φ_r in the three channels. The two pairs of scissors indicate the reducibility of the three Φ_ℓ's. From [27].*

There is a set of 6 "parquet" equations: (1) the actual parquet equation (Fig. 2); (2-4) the Bethe-Salpeter equation in the three channels (in the following we only reproduce the ph channel[2] with $r \in \{d, s\}$ for a symmetric/antisymmetric spin combination)[3]

$$F^{\nu\nu'\omega}_{r,\mathbf{k}\mathbf{k}'\mathbf{q}} = \Gamma^{\nu\nu'\omega}_{r,ph,\mathbf{k}\mathbf{k}'\mathbf{q}} + \sum_{\mathbf{k_1}\nu_1} \Gamma^{\nu\nu_1\omega}_{ph,r,\mathbf{k}\mathbf{k_1}\mathbf{q}}\, G_{\mathbf{k_1}\nu_1}\, G_{(\mathbf{k_1}+\mathbf{q})(\nu_1+\omega)}\, F^{\nu_1\nu'\omega}_{r,\mathbf{k_1}\mathbf{k}'\mathbf{q}}\,; \tag{2}$$

the (5) Dyson Eq. (1); and (6) the Schwinger-Dyson equation which in a four vector notation $k = (\nu, \mathbf{k})$ reads

$$\Sigma_k = -U \sum_{k',q} \left(F_c^{k,k'q} - F_s^{k,k'q}\right) G_{k+q}\, G_{k'}\, G_{k'+q} \tag{3}$$

and connects Σ and F (here for a single-orbital and local interaction U).[4] This set of 6 parquet equations allows us to determine the six quantities F, Φ_r, Σ, and G if we know Λ — or if we approximate it by a local Λ in DΓA. This local Λ can be calculated by solving an Anderson impurity model, similar as in DMFT but on the two-particle level.

In principle, one can then further turn to the $n = 3$-particle level etc.; and for $n \to \infty$ DΓA recovers the exact solution. As a matter of course determining the n=3-particle vertex becomes already cumbersome. But it may serve at least for estimating the error if one is truncating the scheme at the two-particle vertex level. Such an error estimate has been done already for the DF approach [31]. A similar calculation for DΓA is more difficult because one first needs to determine the n=3-particle fully irreducible vertex, whereas the DF approach is based on the full vertex F, which is readily obtained from continuous-time quantum Monte-Carlo simulations [32–34], but a diagrammatically less compact object.

Let us finally mention a simplified ladder DΓA scheme. Here, instead of a local Λ, one starts with a local Γ_{ph} and $\Gamma_{\overline{ph}}$ and uses the Bethe-Salpeter ladder Eq. (2) in these channel to obtain

[2] The frequency-momentum convention is such that the four legs in Fig. 2 have frequency-momentum $k_1 = k$, $k_4 = k'$, $k_2 = k + q$, and, because of energy-momentum conservation, $k_3 = k' + q$.

[3] We assume a proper normalization of the momentum and frequency sums with respect to the number of $\mathbf{k}$-points and β, i.e., $\sum_{\mathbf{k}} 1 = 1$ and $\sum_\nu \widehat{=} \frac{1}{\beta} \sum_\nu$.

[4] There is an additional Hartree(-Fock) term not shown.

F. This way, fluctuations in the particle-particle (Cooperon) channels are neglected. But if we are close to half-filling, or, more specifically, if no superconducting fluctuations nor weak localization is to be expected, the dominant non-local correlations are included in this simplified ladder DΓA. The advantage is that if we do not couple the ladders through the parquet equations, the ladder only depends on a single frequency-momentum q instead of three (q,k,k'). Hence numerically much lower temperatures (finer frequency grids) and much larger momentum grids are feasible. Going further into details would require a chapter on its own, and we refer the reader to [14] and for a pedagogical introduction of DΓA to [27]; for properties of the local two-particle vertex cf. [35].

3 Criticality in the $3d$ Hubbard model

Let us start with the Hamiltonian of the Hubbard model

$$\mathcal{H} = -t \sum_{ij,\sigma} c^\dagger_{i\sigma} c_{j\sigma} + U \sum_i n_{i\uparrow} n_{i\downarrow}, \tag{4}$$

consisting of two terms: a nearest-neighbor hopping amplitude t and a local Coulomb repulsion U. Here $c^\dagger_{i\sigma}$ ($c_{i\sigma}$) creates (annihilates) an electron on site i with spin σ, and $n_{i\sigma} = c^\dagger_{i\sigma} c_{i\sigma}$.
For the study of critical properties in the paramagnetic phase, in particular the behavior of the susceptibility[5] χ and the correlation length ξ is relevant. In the vicinity of the critical temperature T_c, the diverging behavior of χ and ξ is described by critical exponents γ and ν, respectively

$$\chi^{\omega=0}_{\mathbf{Q}} \sim (T - T_c)^{-\gamma}; \tag{6}$$

$$\xi \sim (T - T_c)^{-\nu}. \tag{7}$$

Here, the static ($\omega = 0$) susceptibility is taken for that momentum $\mathbf{q} = \mathbf{Q}$ at which the first divergence occurs at T_c, signaling the emergence of, e.g., ferromagnetic, $\mathbf{Q} = (0, 0, \ldots)$, or antiferromagnetic, $\mathbf{Q} = (\pi, \pi, \ldots)$, order.
In practice the DΓA (or DF) susceptibility is calculated from the full two-particle vertex which describes the connected part of the two-particle Green function. The latter term (often referred to as vertex corrections) in turn together with the disconnected "bubble" diagram yields the susceptibility.[6] This full two-particle vertex includes non-local correlation effects, while the irreducible vertex acting as a building block is local in DΓA.

[5] For the sake of completeness, let us define χ as the Fourier-transform of the spin-spin correlation function from imaginary time τ and lattice sites $\mathbf{R}$ to frequency ω and momentum $\mathbf{q}$ ($\beta = 1/T$: inverse temperature)

$$\chi^{\omega}_{\mathbf{q}} = \int_0^\beta \mathrm{d}\tau \sum_{\mathbf{R}} \langle S^z_{\mathbf{R}}(\tau) S^z_{\mathbf{0}}(0) \rangle \, e^{-i\mathbf{q}\mathbf{R}} \, e^{i\omega\tau} \, . \tag{5}$$

[6] Note that the DMFT calculation of the susceptibility takes the local irreducible vertex in the particle-hole channel and from this constructs the particle-hole ladder [3]. The difference to the ladder DΓA or DF is that the connecting Green functions are recalculated self-consistently or, to mimic this self-consistency effect, a Moriyaesque λ-correction is employed, see [14, 20, 27, 36]. Further, the transversal particle-hole channel is taken into account on an equal footing. In parquet DΓA, additionally, particle-particle vertex corrections couple into the particle-hole and transversal particle hole channel.

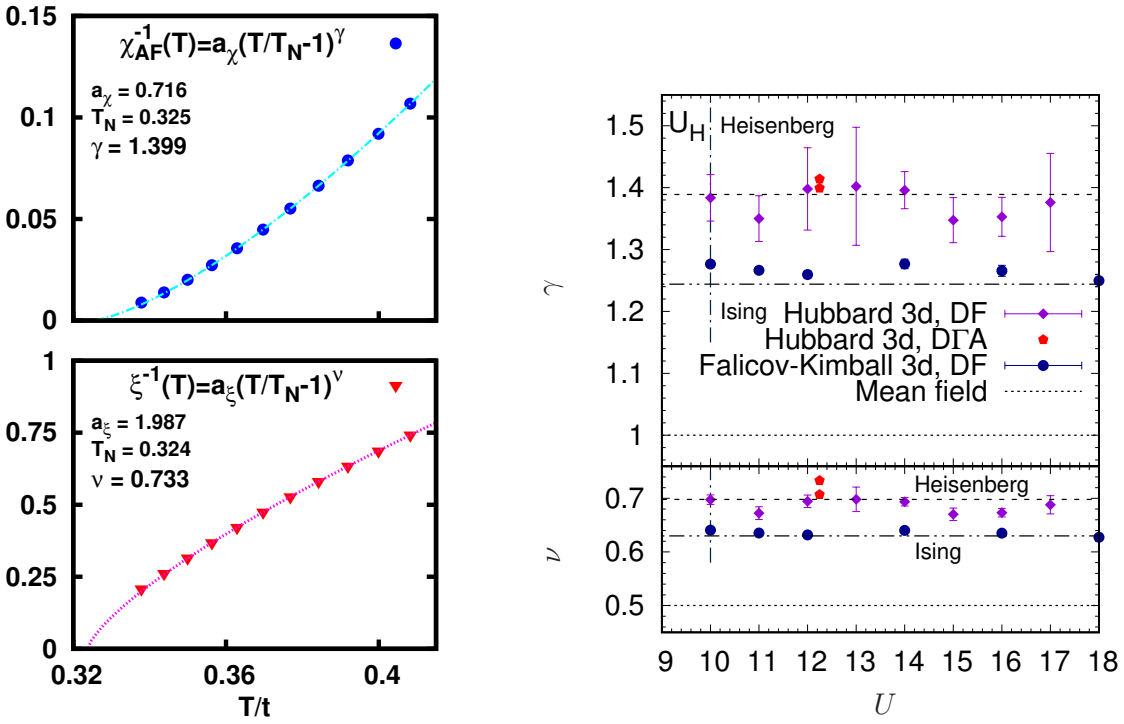

Fig. 3: *Left: Inverse antiferromagnetic susceptibility $\chi^{-1}_{\mathbf{Q}=(\pi,\pi,\pi)}$ (top) and correlation length ξ^{-1} (bottom) as a function of temperature T for the $3d$ Hubbard model at half-filling and $U \approx 12.2t$ in DΓA. Right: Extracted critical exponents obtained in DΓA (from the fits in the left panel) and DF (also for the Falicov-Kimball model) compared to mean-field, $3d$ Heisenberg and $3d$ Ising critical exponents. From Refs. [14–16].*

That is, if we plot the susceptibility $\chi^{\omega=0}_{\mathbf{q}}$ as a function of momentum $\mathbf{q}$, it has a maximum at a certain $\mathbf{q} = \mathbf{Q}$ of value $\chi^{\omega=0}_{\mathbf{Q}}$. The width around this maximum on the other hand is given by the inverse correlation length ξ^{-1} according to the Ornstein-Zernike [37] relation

$$\chi^{\omega=0}_{\mathbf{q}} \sim \frac{1}{(\mathbf{q}-\mathbf{Q})^2 + \xi^{-2}} \,. \tag{8}$$

This relation was found to hold even in a quite large $\mathbf{q}$-region around the maximum $\mathbf{Q}$ so that, in practice, ξ is actually obtained from a fit according to Eq. (8).

Fig. 3 (left panels) plots the thus obtained DΓA susceptibility and correlation length as a function of temperature. There is a clear deviation from a mean-field behavior [$\gamma = 1$, $\nu = 0.5$, see Fig. 4 (a)]. For the temperatures of Fig. 3 (left), $\gamma \approx 1.4$, $\nu \approx 0.7$ is obtained from the indicated numerical fit [15], with the error bar in Fig. 3 (right) corresponding to the deviation to a second fit omitting one temperature point. Within the error bars, this agrees with the critical exponents obtained for the Heisenberg model [$\gamma \approx 1.39$, $\nu \approx 0.705$, see Fig. 4 (b)] for large scale simulations [38]. Indeed universality tells us that the two models should have the same critical exponents since the dimension is the same ($3d$), as is the symmetry of the order parameter: $O(3)$ since we have rotational symmetry as regards the possible orientation of the ordered magnetic moment.

Let us also note that the two exponents are connected through the Fisher relation [39] as

$$\gamma/\nu = 2 - \eta \tag{9}$$

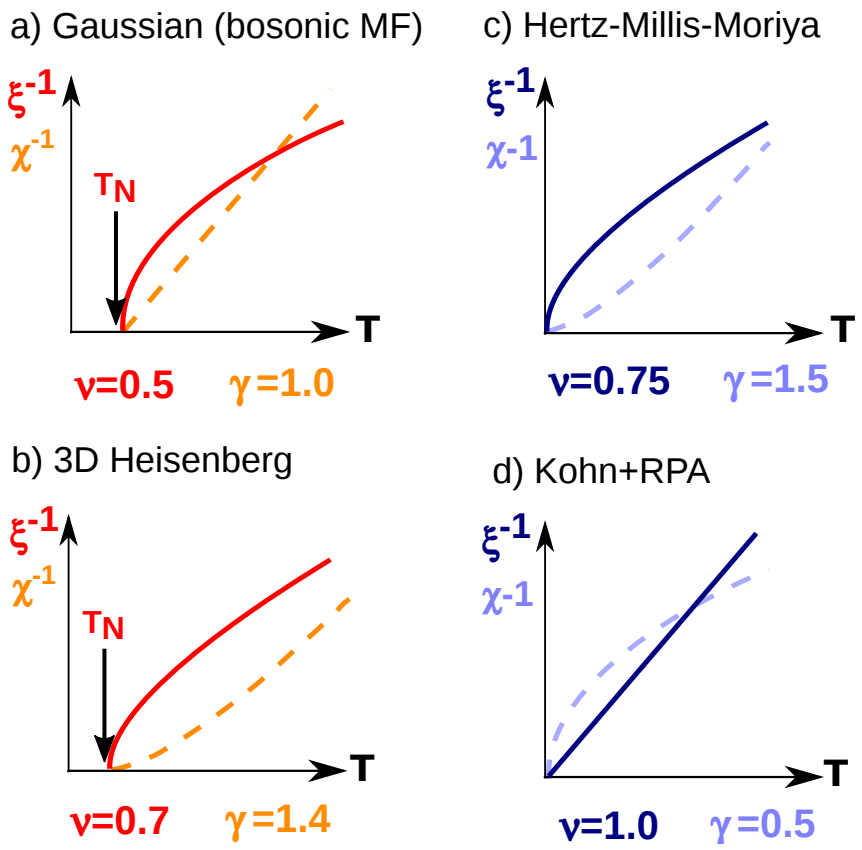

Fig. 4: *Inverse susceptibility χ^{-1} and correlation length ξ^{-1} as a function of temperature T. Left: Classical critical point with a finite critical temperature T_N, comparing a) Gaussian fluctuations and b) the $3d$ Heisenberg model. Right: Quantum critical point with a phase transition at $T = 0$, comparing c) conventional Hertz-Millis-Moriya theory and d) the Kohn-line universality class. From Ref. [18].*

with the critical exponent η describing the decay of spatial correlations at $T = T_c$. The exponent η vanishes above the upper critical dimension, and is typically very small $\eta \approx 0$ in 3D and even in 2D. Hence, we will further consider $\eta = 0$ in these Lecture Notes.

While the deviation from mean-field exponents is obvious, one should always keep in mind that the fitting procedure to extract critical exponents from numerical as well as from experimental data has a large degree of uncertainty [40, 41]. Further there is, necessarily, some distance of the numerical data to the critical temperature.[7] Hence "last minute" changes of the curvature in the immediate vicinity of the critical temperature might be missed in a numerical fit. For the attractive Hubbard model, whose superconducting phase transition out of half-filling should have the universality class of the XY model, it was found [42] that the critical exponents might also be consistent with $\gamma = 2$, $\nu = 1$ close to T_c. At the same time, other groups obtained the same critical $3d$ Heisenberg exponents using the DF approach [16], and different ones for the Falicov-Kimball model [17]. which has an Ising universality class, see Fig. 3 (right panel).

[7] As the correlation length keeps increasing to thousands and ten thousands of lattice sites, we need a larger and larger numerical resolution in Fourier, i.e. $\mathbf{k}$, space. Doing reliable calculations significantly closer to T_c than shown is hardly possible.

4 Quantum criticality in the $3d$ Hubbard model

A quantum critical point (QCP) is a critical point at zero temperature, $T = 0$. In this case, besides the classical fluctuations with long-range correlations in space, an additional dimension, time, becomes relevant. At any finite temperature, these correlations in time are not relevant since they are cut-off at a scale $\beta = 1/T$. Maybe one can best understand this in imaginary time τ as it is restricted to the interval $\tau \in [0, \beta]$.

For a classical critical point at finite T, the correlation length in time will hence eventually exceed $\beta = 1/T$ if we are close enough to the phase transition. At this point, correlations in time are cut off, and not relevant any longer close enough to the phase transition. Consequently, the critical exponents are only determined by the number d of spatial dimensions and the symmetry of the order parameter.

This changes for a quantum phase transition at $T = 0$. Here, also a divergent correlation length in time becomes relevant. The effective dimension is hence $d_{\text{eff}} = d + z$. With the above argument, one might assume one extra dimension, i.e., $z = 1$. However, fluctuations in time can also lead to other values of the dynamical critical exponent z. This is because the spatial correlation length diverges as $\xi \sim T^{\nu}$ at a QCP whereas the correlation length in time behaves as $\xi_\tau \sim T^{z\nu}$. Depending on the kind of ordering and the dimension, z may vary. For example, we have $z = 1$ for an insulating and $z = 2$ for a metallic antiferromagnetic QCP. For a review see [43].

The standard theory for quantum critical points and exponents is the Hertz-Millis-Moriya theory [44–46], based on weak coupling ladder diagrams in a perturbative renormalization group. Experimentally, on the other hand, quantum criticality is best studied in heavy fermion systems. That is, in strongly correlated electron systems with f-electrons for which a weak coupling theory is certainly not sufficient. This has led to different proposals and further theories. One theory that takes strong electronic correlations into account and the breakdown of the f-electron Fermi surface is the so-called local quantum criticality, see e.g. [47]. This theory is based on the extended DMFT [48, 49] which considers the local correlations and self-energy emerging from non-local interactions, here considered to arise from non-local spin fluctuations.

Diagrammatic extensions of DMFT such as the DΓA take both kinds of physics into account: similar diagrams as in Hertz-Millis-Moriya theory but with the local vertex instead of a bare interaction as a starting point so that DMFT effects of strong correlations are automatically included; and they inherently allow us to describe breakdowns of Fermi surfaces as well.

Let us now turn to quantum criticality in the $3d$ Hubbard model. Because of perfect nesting we have an antiferromagnetic ground state for all interactions U at half-filling. Thus, we need to find another way to realize a quantum critical point. One possibility is to dope the system as shown in Fig. 5. With doping the antiferromagnetic order is suppressed so that we eventually arrive at a quantum critical point (QCP) at $n \approx 0.8$. A further complication arises however: The second order phase transition is only towards a commensurate Néel antiferromagnetic ordering with wave vector $\mathbf{Q} = (\pi, \pi, \pi)$ close to half filling (open triangles in Fig. 5). With further doping and at the QCP it is towards an incommensurate antiferromagnetic ordering with $\mathbf{Q} =$

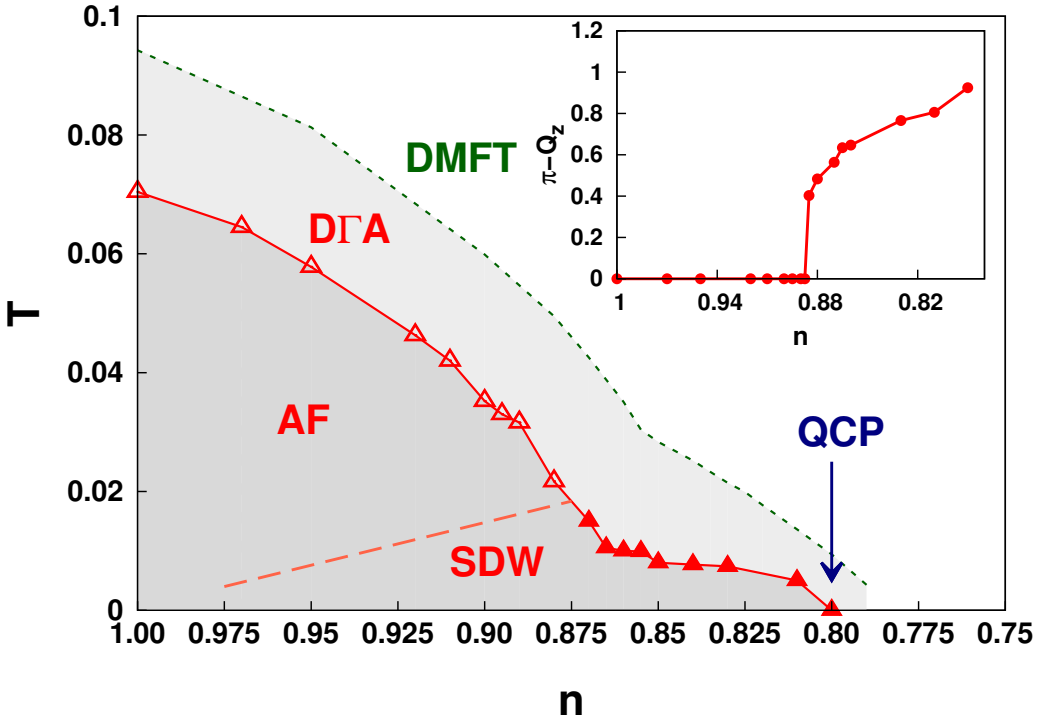

Fig. 5: *Phase diagram of the* $3d$ *Hubbard model at* $U = 4\sqrt{6}t \approx 9.8\ t$*, showing the antiferromagnetic critical temperature as a function of electron filling* n *in DMFT (green dashed line) and DΓA (red triangles). Inset: The antiferromagnetic ordering wave vector* $\mathbf{Q}$ *is commensurate with* $Q_z = \pi$ *(open triangles in the main panel) around half-filling and incommensurate with* $Q_z < \pi$ *ordering at larger doping (full triangles in the main panel). The dashed line of the main panel indicates the possible crossover between commensurate and incommensurate* Q_z *in the ordered phase. From Ref. [18].*

$(\pi, \pi, \pi - \delta)$ (filled triangles in Fig. 5). Besides this interesting aspect of the changing $\mathbf{Q}$ vector (cf. inset of Fig. 5), we also see that the spin fluctuations taken into account in the DΓA suppress the critical temperature compared to the DMFT solution.

In Fig. 6 we study the critical exponents again for both, the susceptibility χ and correlation length ξ. For $n = 1$ and $n = 0.87$ we are far away from the QCP in Fig. 5, and within the numerical error bars our fit suggests the classical critical exponents of the Heisenberg model ($\nu \approx 0.7$, $\gamma \approx 1.4$). The dopings $n = 0.805$ and $n = 0.79$ are just below and above the QCP in Fig. 5. Here, the critical exponent for the correlation length ξ clearly shows a different exponent; within the error bars we obtain $\nu \approx 1$. Only at the lowest temperature there is a deviation to a smaller ξ^{-1} for $n = 0.805$, signaling the eventual finite-temperature antiferromagnetic phase transition as we are still to the left of the QCP in Fig. 6. At $n = 0.79$, on the other hand, we are to the right of the QCP. That is, eventually the correlation length must saturate because of the paramagnetic ground state. Indeed, here the value at the lowest T in Fig. 6 indicates a deviation to a larger ξ^{-1}.

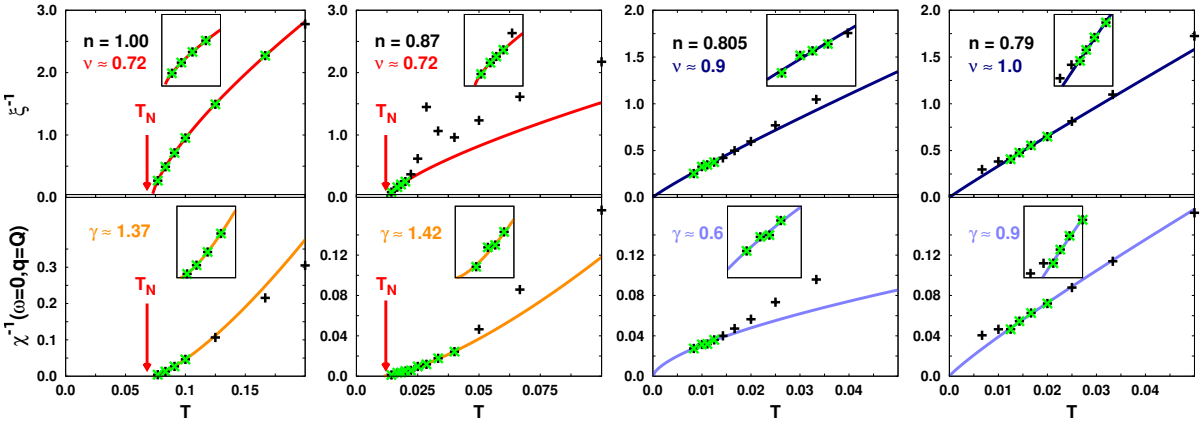

Fig. 6: *Inverse correlation length (ξ^{-1}, upper panels) and susceptibility (χ^{-1}, lower panels) vs. T in DΓA for different n. Solid lines: fits for extracting the critical exponents γ and ν from the green points. Insets: zoom in to the lowest temperature points. From Ref. [18].*

The result $\nu \approx 1$ was quite a surprise at first. Since our effective dimensions is $d_{\text{eff}} = d + z = 3 + 2 > 4$ we are above the upper critical dimension four[8] and one should expect the behavior of a bosonic mean-field theory with $\nu = (d + z - 2)/(2z) = 3/4$ according to Hertz-Millis-Moriya theory, see Fig. 4c). By analytical calculations in the random phase approximation (RPA) it was shown [18] that one obtains the exponents of a different universality class instead. This is caused by peculiarities of the Fermi surface. More specifically, there are Kohn-lines on the Fermi surface of the doped Hubbard model which are separated by an incommensurate wave vector and have opposite Fermi velocities, see Fig. 7. These lines give rise to the so-called Kohn anomalies in the phonon spectrum [50] if we take phonons and the electron-phonon coupling into account.

In the case of a QCP they give rise to particularly strong transversal spin fluctuations which eventually lead to the exponents $\nu = 1$ and $\gamma = 0.5$, see Fig. 4d) [18]. Note, that their ratio ($\nu = 2\gamma$) is just the opposite, as to be expected from the Fisher relation Eq. (9) which for $\eta \approx 0$ yields $\nu = \gamma/2$. While the numerical error bar for determining γ in Fig. 6 is considerably larger than for ν,[9] it is save to say that also numerically $\nu > \gamma$ in DΓA instead of the expected behavior $\nu = \gamma/2 < \gamma$ without Kohn lines.

In case of a finite temperature classical critical point, the Kohn anomalies are not relevant because the Fermi surface effect is broadened out by a finite self-energy at the Fermi energy. If we add a finite next-nearest neighbor hopping t' on the other hand, there are no full Kohn lines any longer. But individual Kohn points with opposite Fermi velocities still occur quite generically. We expect such points to lead to a further, different, universality class for the critical exponents ($\gamma = \nu = 1$).

[8] The marginal case of $d_{\text{eff}} = 4$ requires special considerations.

[9] as can be seen from the somewhat different fitted values for $n = 0.805$ and $n = 0.79$

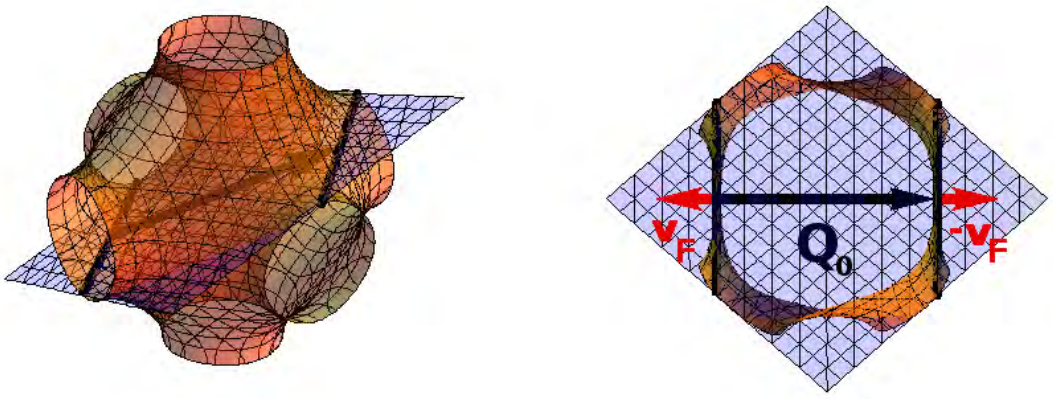

Fig. 7: *Left: Visualization of the parallel Kohn lines (black lines) on the Fermi surface of the $3d$ Hubbard model with nearest neighbor hopping. Right: Two-dimensional cut as indicated in the left panel, showing the connecting wave vector $\mathbf{Q}_0$ (black arrow) and the opposite Fermi velocities $\mathbf{v}_F$ (red arrows). From Ref. [18].*

5 Quantum criticality in the $2d$ periodic Anderson model

With the additional dimensions z brought about by the temporal correlations, it is not that simple to remain below the upper critical dimension $d = 4$. Hence, we next study the $2d$ case and another model, the periodic Anderson model (PAM)

$$\mathcal{H} = \sum_{\mathbf{k},\sigma} \varepsilon_{\mathbf{k}}\, d^\dagger_{\mathbf{k}\sigma} d_{\mathbf{k}\sigma} + \varepsilon_f \sum_{i\sigma} f^\dagger_{i\sigma} f_{i\sigma} + U \sum_i n_{f,i\uparrow} n_{f,i\downarrow} + V \sum_{i,\sigma} \left(d^\dagger_{i\sigma} f_{i\sigma} + f^\dagger_{i\sigma} d_{i\sigma} \right). \qquad (10)$$

This Hamiltonian can be considered as the simplest model for an f-electron system where we have two different kinds of electrons: Localized f-electrons with creation (annihilation) operators $f^\dagger_{i\sigma}$ ($f_{i\sigma}$), and $n_{f,i\sigma} = f^\dagger_{i\sigma} f_{i\sigma}$. These interact by a local Coulomb repulsion U and feel a local one-particle potential ε_f. Further, there are itinerant d-electrons [$d^\dagger_{i\sigma}$ ($d_{i\sigma}$)] with hopping t from site to site, or alternatively with an energy-momentum dispersion relation $\varepsilon_{\mathbf{k}}$. Finally, there is a hybridization V between both kinds of electrons. The difference to the single impurity Anderson model is that there is not only a single site of interaction but a periodic array of sites. If we consider the strong coupling limit $U \gg V$ of the periodic Anderson model in the particle-hole symmetric case of half-filling ($\mu = 0$, $\epsilon_f = -U/2$), we have an average filling of one f- and d-electron per site. Because of the strong interaction, the f-sites are single-occupied, i.e., they can be considered as a spin. In second order perturbation theory there is a coupling $J = 4\, V^2/U$ between this localized spin and the spin-operator for the conduction electrons. That is, we can map the periodic Anderson model onto a Kondo lattice model in the strong coupling limit.

This Kondo lattice model and hence the periodic Anderson model has two competing phases: On the one hand there is the Kondo effect that we also know from the (single-site) Kondo model. At high temperatures, we have free spins and a Curie susceptibility $\chi \sim T^{-1}$. Below the Kondo temperature, T_K an additional Abrikosov-Suhl resonance develops at the Fermi energy, and the

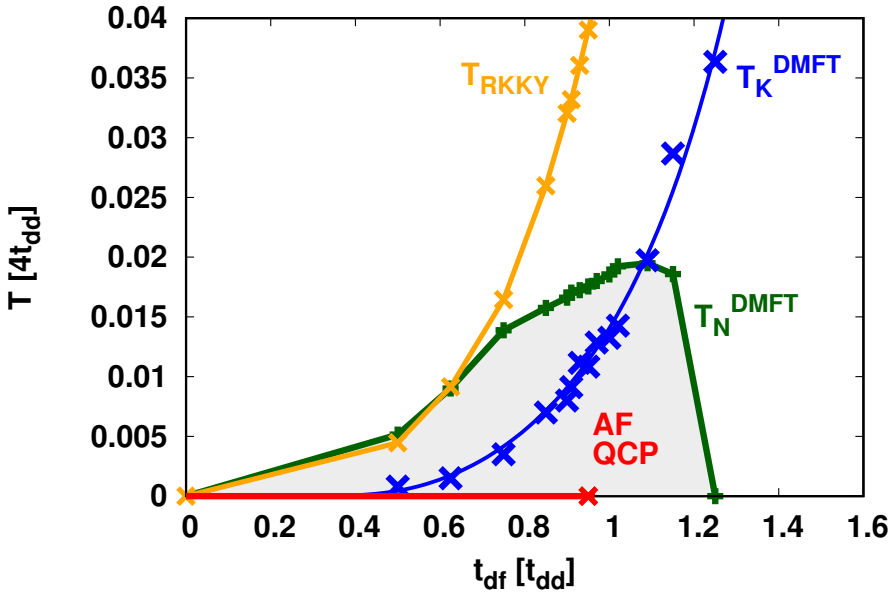

Fig. 8: *Phase diagram temperature T vs. hybridization $t_{df} \equiv V$ of the $2d$ half-filled periodic Anderson model at $U = 4t_{dd}$ (nearest-neighbor d-d hopping). The figure shows the antiferromagnetic transition line in DMFT (green) and DΓA (red), the DMFT Kondo-temperature T_K^{DMFT} (blue), and T_{RKKY} (yellow). From [19].*

spin is screened. In the particle-hole symmetric case of half-filling, this Kondo resonance is however somewhat special: We have a renormalization of the following (non-interacting) situation: There is a flat f-band at the Fermi energy E_F in the middle of the dispersive conduction band. If we now switch on the hybridization a gap opens at the band crossings at E_F. This hybridization gap at E_F leads to an insulator not only for the non-interacting model, but also if we have a renormalized picture thereof due to the Kondo effect. This phase is hence called a Kondo insulator.

For the (single-site) Kondo model

$$T_K \sim e^{-1/(2\rho(0)J)} \tag{11}$$

with non-interacting density of states $\rho(0)$ [51], and also for the PAM we get a Kondo temperature of similar magnitude, in particular an exponential scaling; see e.g. [52] for DMFT calculations revealing an actually somewhat enhanced T_K in the PAM.

Competing with the Kondo effect is a magnetic phase. For understanding this magnetic ordering, we can envisage the magnetic Ruderman-Kittel-Kasuya-Yosida (RKKY) coupling in perturbation theory: An f-electron spin is coupling with amplitude J to the conduction electrons. These are however not immobile and carry the spin information to neighboring sites with an amplitude given by the (non-interacting) susceptibility χ_0. On another site, the conduction electron couples again with the localized f-spin on that site, so that we altogether get the following coupling strength or critical temperature for the magnetic ordering:

$$T_{RKKY} \sim J^2 \chi_{0,\mathbf{Q}}^{\omega=0}. \tag{12}$$

In our case, the maximal coupling is for the antiferromagnetic wave vector $\mathbf{Q} = (\pi, \pi)$ and this magnetic ordering opens a gap at ε_F so that we have an insulating antiferromagnetic phase.

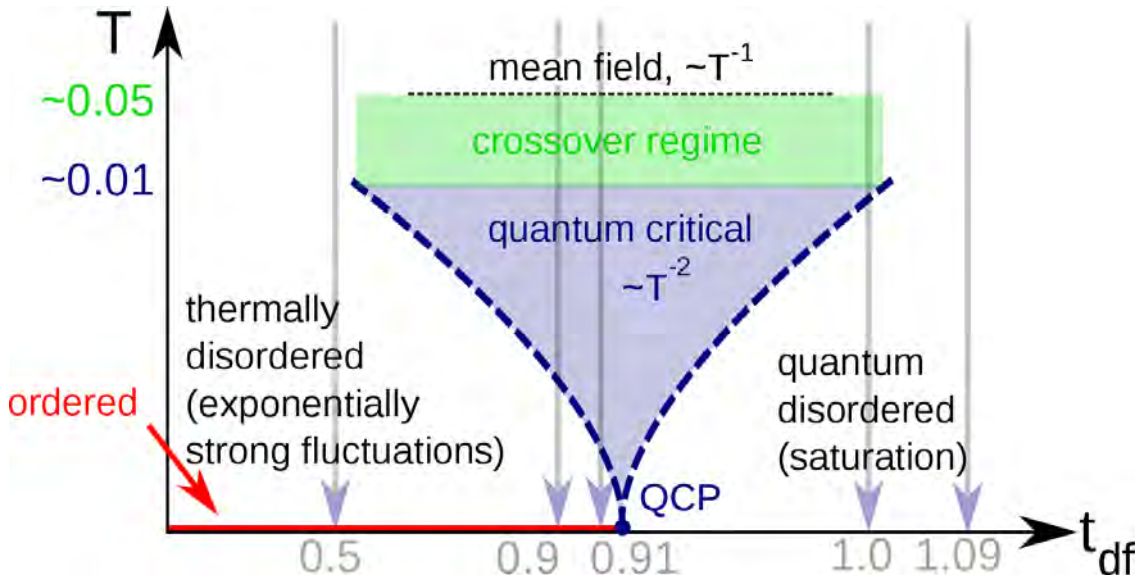

Fig. 9: *Schematics of the quantum critical region with a scaling $\chi \sim T^{-2}$ above the quantum critical point of Fig. 8. From [19].*

Since T_K is exponentially small for small J, cf. Eq. (11), $T_{RKKY} > T_K$ and we get an antiferromagnetic insulator at small J. But with increasing J, at some point the Kondo effect wins, and there is a phase transition to a Kondo insulator without long-range order at $T_K \approx T_{RKKY}$. Plotting T_{RKKY} and T_K vs. V, one obtains the famous Doniach [53] phase diagram.

In Fig. 8, we show the corresponding phase diagram as obtained using DMFT[10] and DΓA. Note that in DMFT, $T_{RKKY} \sim J^2 \sim V^4$ only holds for small V; for larger values of V this second order result is no further applicable. If the DMFT Kondo temperature[11] T_K becomes of the order of the DMFT antiferromagnetic ordering temperature, antiferromagnetism breaks down, and we have a Kondo insulator instead at a finite critical V_c. That is, we have a quantum critical point between a Kondo insulator at large V and an antiferromagnetic insulator at small V.

The DΓA phase diagram in Fig. 8 is distinctively different. Non-local correlations, i.e., specifically antiferromagnetic spin fluctuations, suppress the antiferromagnetic ordering. Since we are in $2d$, this suppression is particularly strong and DΓA respects the Mermin-Wagner theorem [55]: long-range antiferromagnetic order only survives at $T = 0$.[12] Nonetheless, we have a QCP which we further analyze in the following.

Above the QCP, there is a quantum critical region where exponents of the susceptibility and correlation length are governed by the QCP, i.e., temporal fluctuations are relevant, see Fig. 9. For the QCP of a $2d$ antiferromagnetic insulator we expect the same exponents as for the $2d$ Heisenberg model, i.e., $\chi \sim T^{-2}$, $\gamma = 2$ (and with Eq. (9) $\nu = \gamma/2 = 1$ for $\eta \approx 0$) [56]. In contrast, for high temperatures we expect the Curie behavior $\chi \sim T^{-1}$ for free spins.

[10] For the DMFT phase diagram of the Kondo lattice model see [54].
[11] determined from the maximum of the local susceptibility as a function of T
[12] Cf. [20] for the fulfillment of the Mermin-Wagner theorem for the $2d$ Hubbard model in DΓA.

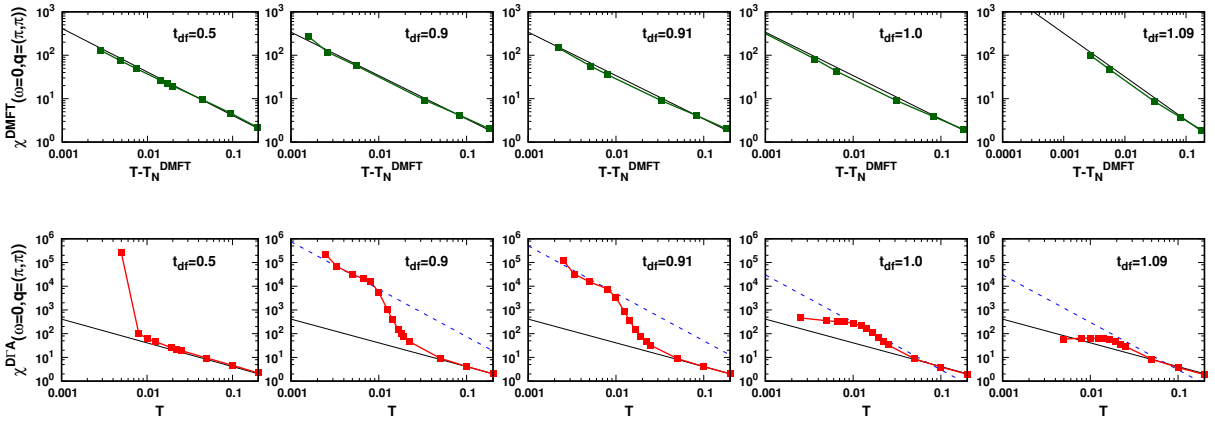

Fig. 10: *Magnetic susceptibilities vs. temperature on a double logarithmic plot in DMFT (top panels, green) and DΓA (bottom panels, red) for different hybridization strengths $t_{df} = V$. The black solid and blue dotted lines indicate a $\chi \propto T^{-1}$ and $\chi \propto T^{-2}$ behavior, respectively. From [19].*

The behavior of the susceptibility $\chi \sim T^{-\gamma} \sim T^{-2}$ and related correlation length $\xi \sim T^{-\nu} \sim T^{-1}$ in the quantum critical region can be rationalized as follows: First, the conjectured mapping onto a non-linear σ model [57] and quantum Monte Carlo data for the Heisenberg model [58] suggest a dynamical critical exponent $z = 1$. Further, in the quantum critical region, temperature sets a cut-off $1/T$ to the correlation length in time: $\xi_\tau \lesssim 1/T$. Finally with $\xi \sim T^{-\nu}$ and $\xi_\tau \sim T^{-z\nu}$, we have $\xi \sim \xi_\tau^{1/z} \sim T^{-1}$ for $z = 1$.

Fig. 10 shows that DΓA is indeed able to resolve such a complex behavior and the quantum critical exponent $\gamma = 2$ with a crossover towards $\gamma = 1$ at high temperatures. DMFT does not include spatial correlations and hence shows a $\chi \sim T^{-1}$ (i.e., $\gamma = 1$) behavior in the whole temperature range.

For low T and $V < V_C$ eventually antiferromagnetic order sets in. While true long range antiferromagnetic order only sets in at $T = 0$, we have already an exponentially large correlation length and susceptibilities at finite T. These will eventually dominate, setting an end to the quantum critical region. Indeed for such parameters the DΓA results of Fig. 10 show a deviation to even larger susceptibilities at the lowest temperature.

For low T and $V > V_C$, on the other hand, eventually a Kondo insulating phase develops (quantum disordered phase in Fig. 9). Because this is a gapped (renormalized) band insulator with a hybridization gap, we expect that here the susceptibility eventually vanishes. Indeed for such parameters the DΓA results of Fig. 10 show a deviation to smaller susceptibilities at lower temperatures. A full suppression of the susceptibility because of the Kondo gap was only found at larger V (not shown); but it is also expected at $t_{df} = V = 1.09$ but only for even lower temperatures.

6 Superconductivity in the $2d$ Hubbard model

In this section we would like to leave the question of critical exponents behind and discuss instead the prospects of superconductivity in the $2d$ Hubbard model. There are different ways how superconductivity might arise. But non-local correlations are the key; DMFT cannot describe d-wave superconductivity. One possibility is through antiferromagnetic spin fluctuations. These do not only lead to a pseudogap in diagrammatic extensions of DMFT [23, 20, 25] but may also act as a pairing glue for superconductivity [59].

Since antiferromagnetic spin fluctuations emerge from the particle-hole channel and superconductivity is an instability of the particle-particle channel,[13] one needs in principle the parquet equations for describing this interplay. The drawback is that solving these equations requires a much larger effort than solving the ladder equation in a specific channel. This restricts the available temperature range, and even if it is called "high-temperature" superconductivity the typical T_c is still quite low compared to room temperature. We will later present such parquet DΓA calculations, but here the lowest possible temperatures are actually not low enough to unambiguously identify a phase transition into a superconducting phase. Such parquet DΓA can yield, however, the leading superconducting instability and the trend that superconductivity prevails over antiferromagnetism for large enough dopings.

Before turning to these parquet results, let us instead first discuss a poor man's variant of such a parquet equation [60]. Here, from a local vertex $\Gamma^{\nu,\nu',\omega}_{\sigma\sigma'}$, irreducible in the particle-hole channel, first the non-local vertex $F^{k,k',q}_{\sigma\sigma'}$ is calculated via the Bethe-Salpeter ladder in the particle-hole and transversal particle-hole channel. This F includes spin-fluctuation; and is in turn also used to calculate Σ_k. Up to this point it is a conventional ladder DΓA calculation.

But in the next step we use this F to calculate a non-local vertex irreducible in the particle-particle channel: $\Gamma^{k,k',q=0}_{\rm pp} \equiv F^{k',-k,k-k'} - \Phi^{\nu,\nu',\omega=0}_{\rm pp}$, where all particle-particle reducible diagrams $\Phi_{\rm pp}$ of F are subtracted and again a four-vector notation is used. With this $\Gamma_{\rm pp}$ we solve the particle-particle ladder or the simplified linearized gap (Eliashberg) equation

$$\lambda v_k = -\sum_{k'} \Gamma^{k,k',q=0}_{\rm pp}\, G_{k'}\, G_{-k'}\, v_{k'}, \tag{13}$$

where λ and v_k are the eigenvalue and eigenvector in the particle-particle channel, respectively. This is like a single parquet step, where we insert one channel (the particle-hole and transversal particle-hole) into another (the particle-particle). In a full parquet we would also turn back from the particle-particle to the particle-hole channel.

Physically Eq. (13) is akin to the standard random phase approximation (RPA) ladder which yields

$$\chi = \chi_0/(1 + U\chi_0) \tag{14}$$

but with the momentum and frequency dependent $\Gamma^{k,k',q=0}_{\rm pp}$ instead of U. If the leading eigenvalue λ of $-U\chi_0$ [or here of $-\Gamma_{\rm pp}\chi_0$] approaches one [$\lambda \to 1$], Eq. (14) diverges and superconductivity sets in.

[13] also coined Cooperon channel

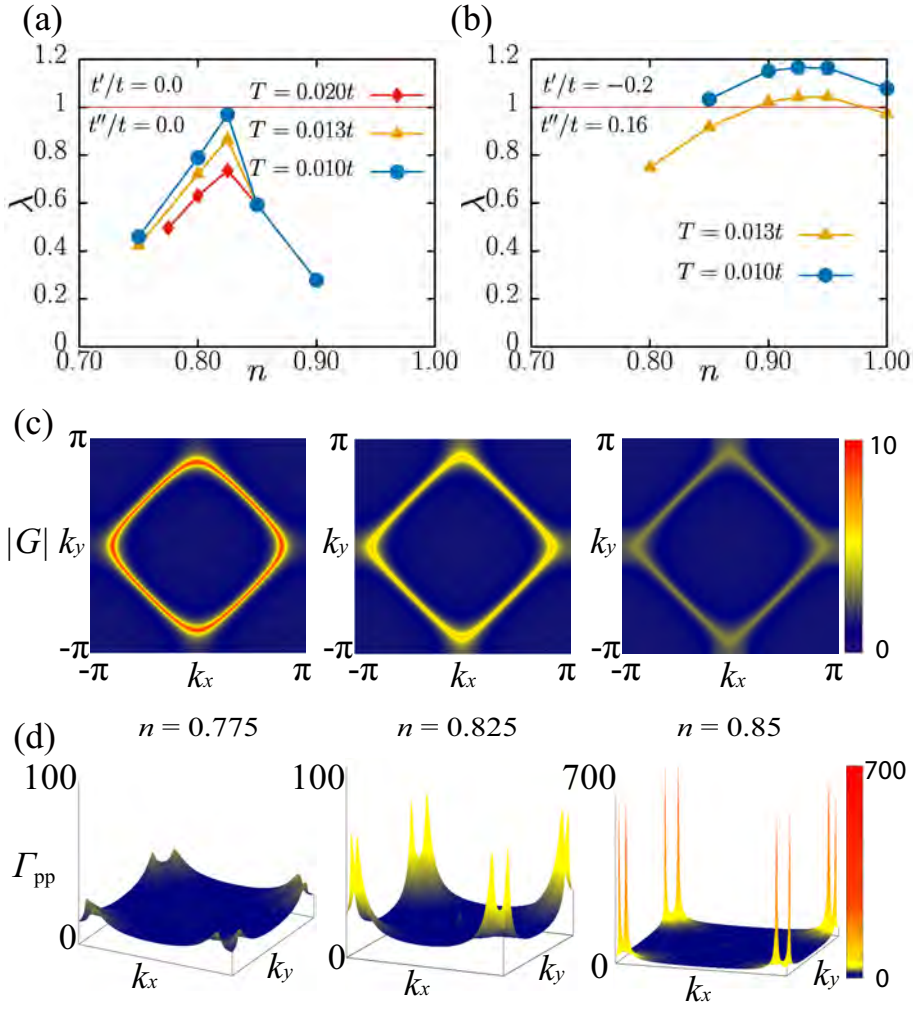

Fig. 11: *Leading d-wave eigenvalue λ against band filling n for $U = 6t$, $T/t = 0.010$, 0.013, 0.020 with (a) $t' = t'' = 0$ and (b) $t'/t = -0.20$, $t''/t = 0.16$. (c) Momentum dependence of the Green function $|G_{\pi/\beta,\boldsymbol{k}}|$, and (d) the pairing interaction vertex $\Gamma_{\rm pp,\boldsymbol{Q}=(\pi,\pi)}$ for $n = 0.775$ (overdoped), 0.825 (optimally doped), and 0.85 (underdoped), at $T/t = 0.02$ and further parameters as in (a). From [60].*

Fig. 11 shows the leading superconducting eigenvalue which is of d-wave symmetry and approaching $\lambda = 1$ at $T_{\rm c} \lesssim 0.01t$ for nearest-neighbor hopping (t) only [Fig. 11(a)]. At this $T_{\rm c}$ the superconducting susceptibility diverges. If next- (t') and next-next-nearest neighbor hoppings (t'') are included with parameters adjusted to the bandstructure of Hg-based cuprates we get a somewhat larger $T_{\rm c} \approx 0.015t$ [Fig. 11(b)]. If we translate this into Kelvin, by taking a typical hopping parameter $t \approx 0.45\,$eV, this corresponds to $T_{\rm c} \approx 50 - 80$ K for a filling of $n = 0.80 - 0.95$. These are very reasonable T_c values for cuprates, in particular if one takes into account that no further optimization with respect to t' and t'' has been done.

Fig. 11 also reveals a superconducting dome. This is the consequence of two opposing effects: On the one hand, stronger antiferromagnetic spin fluctuations towards half-filling increase the superconducting pairing glue $\Gamma_{\rm pp}^{k,k',q=0}$ in Fig. 11(d) so that T_c would increase towards half-filling. But at the same time the spin-fluctuations suppress the Green function which also enters

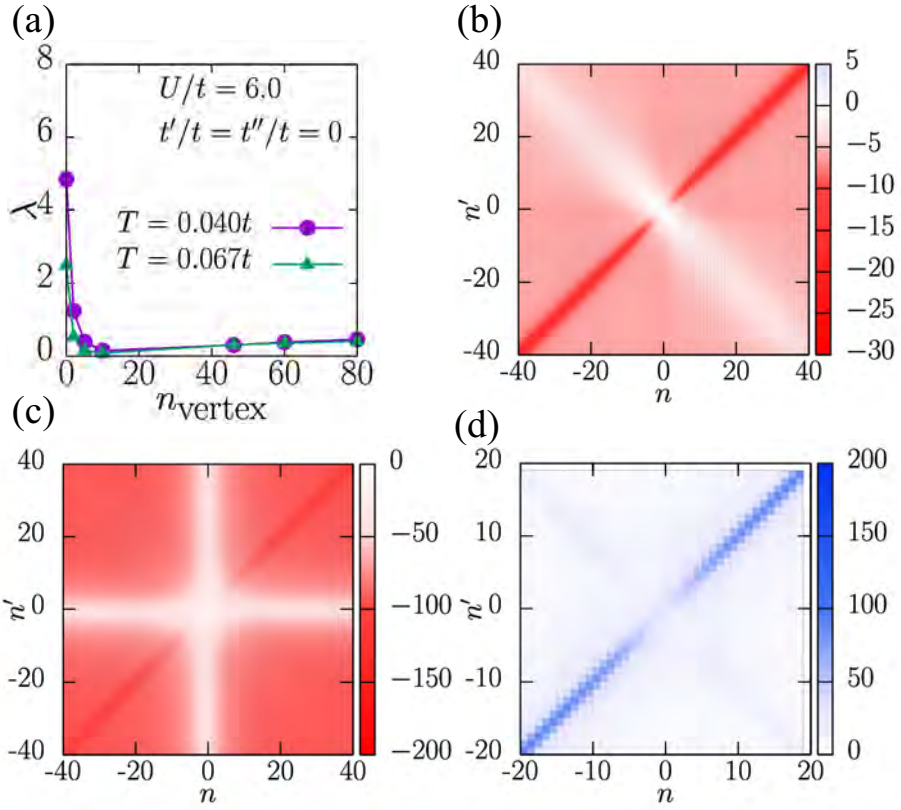

Fig. 12: *(a) Eigenvalue λ against the frequency range n_{vertex} over which the local vertex structure of in the magnetic channel $\Gamma_{\mathrm{m}}(\nu_n, \nu_{n'}, \omega = 0)$ (shown in panel b) is considered. (c) Full vertex $F_{\mathrm{m},\boldsymbol{Q}=(\pi,\pi)}(\nu_n, \nu_{n'}, \omega = 0)$ and (d) pairing interaction $\Gamma_{\mathrm{pp},\boldsymbol{Q}=(\pi,\pi)}(\nu_n, \nu_{n'}, \omega = 0)$. The parameters are: $U = 6t, t' = t'' = 0, n = 0.825$ and $T/t = 0.040, 0.067$. From [60].*

in the Eliashberg Eq. (13). Eventually this leads even to the development of a pseudogap, but for the parameters of Fig. 11(c) only a suppression of $|G_k|$ towards half-filling is visible. This Green function effect suppresses T_c. The balance of both effects yields the dome-like structure. A superconducting dome has also been reported in e.g. [61, 62, 26, 63], but not in the dual-fermion approach [64, 21] or in Ref. [65].

Kitatani *et al.* [60] were further able to point out that the dynamics of the vertex, i.e., its frequency structure plays a pivotal role for T_c. That is, the vertex dynamics suppresses T_c by one order of magnitude. Without this suppression room temperature superconductivity would be possible.

Fig. 12(b) shows the local vertex Γ_{m} that serves as starting point for the DΓA calculation. Clearly, it is suppressed at the lowest frequencies. This low frequency suppression is also seen in the non-local full vertex $F_{\mathrm{m},\boldsymbol{Q}}$ that is calculated from Γ_{m} and shown in Fig. 12(c). That is, antiferromagnetic spin fluctuations are suppressed for small frequencies. Not surprisingly also the superconducting pairing glue, i.e., the non-local vertex irreducible in the particle-particle channel in Fig. 12(d) is suppressed.

Fig. 12(a) shows the values of the superconducting eigenvalue λ that we had without this suppression of the vertex. More precisely, the λ that we would have if we replaced the local vertex of Fig. 12(b) by its static limiting value $\Gamma_{\mathrm{m}}^{\nu_n,\nu_{n'},\omega=0} = -U$ for Matsubara frequencies $|\nu_n|$, $|\nu_{n'}|$, $|\omega| > n_{\mathrm{vertex}}$. For $n_{\mathrm{vertex}} = 0$, we have $\Gamma_{\mathrm{m}}^{\nu_n,\nu_{n'},\omega=0} = -U$ at all frequencies and an order of

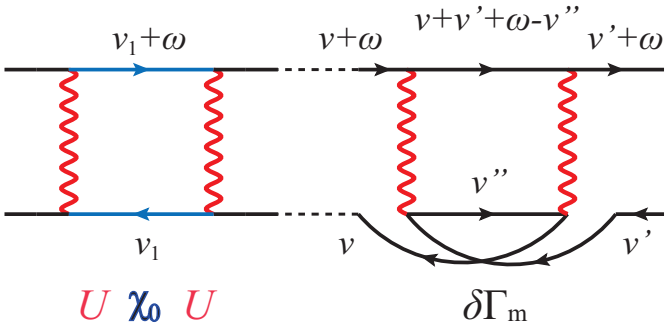

Fig. 13: *Left part of the diagram: a typical RPA ladder diagram in the particle-hole channel with building block U (red wavy line) and χ_0 (two blue Green functions with fermionic frequencies ν_1 and $\nu_1 + \omega$). Right part of the diagram: Local (second-order) vertex correction $\delta\Gamma_{\rm m}$ with a* particle-particle *bubble. From [60].*

magnitude larger λ in Fig. 12(a); for $n_{\rm vertex} \to \infty$ we recover the proper DΓA result. Not only λ is enhanced but along with it also T_c from about 0.01t to 0.13t.

In this situation it is imperative to identify the physical processes that are responsible for the suppression of $\Gamma_{\rm m}$ in Fig. 12(b). Analyzing diagrams order by order, Kitatani *et al.* [60] found that already the second order particle-particle diagram as displayed in Fig. 13 (right part) is the main driving force for the suppression of $\Gamma_{\rm m}$ in Fig. 12(b). From Fig. 13 we also see that the particle-particle bubble becomes maximal for $\nu + \nu' + \omega \approx 0$. Note that $\omega = 0$ in Fig. 12(b), so that the suppression is maximal at $\nu = -\nu'$ in Fig. 12(b). These particle-particle screening processes explain the substantial suppression of the local $\Gamma_{\rm m}$ and hence of antiferromagnetic spin fluctuations and the superconducting pairing glue Γ_{pp} for lowest frequencies.

Having identified this oppressor of high temperature superconductivity, a screening of antiferromagnetic spin fluctuations by local particle-particle bubbles, gives us some hope to find new ways of enhancing T_c, possibly to room temperature and beyond. However, this is only the first step, getting rid of (a large) particle-particle screening is not at all trivial, and remains a challenge for the future.

Superconductivity in parquet DΓA

Finally, we would like to turn to the more complete parquet DΓA. As already mentioned, this means that we have to do calculations at higher temperatures, considerably above T_c. Fig. 14 shows the parquet DΓA result for a filling $n = 0.85$ where we have d-wave superconductivity in Fig. 12. Indeed, in this parameter range Kauch *et al.* find that d-wave superconductivity is the leading instability in the (superconducting) particle-particle channel, seemingly surpassing the magnetic instability at lower temperatures. For this doping, the magnetic susceptibility is still peaked at $\mathbf{Q} = (\pi, \pi)$ in Fig. 14 (left). This antiferromagnetic wave vector $\mathbf{Q} = (\pi, \pi)$ naturally connects the positive [at $\mathbf{k} = (\pm\pi, 0)$] and negative [at $\mathbf{k} = (0, \pm\pi)$] regions of the superconducting d-wave eigenvector in Fig. 14 (middle panels), as is needed for the Eliashberg Eq. (13) to realize an eigenstate for a repulsive interaction. Fig. 14 (right) displays the same

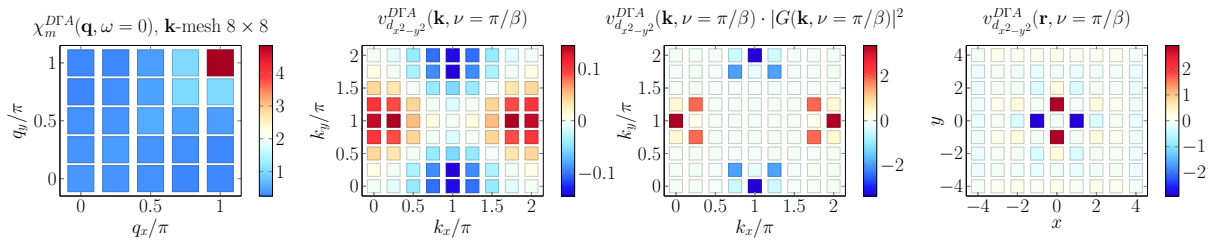

Fig. 14: *Left: Magnetic susceptibility* $\chi_m(\mathbf{q},\omega=0)$ *vs.* q_x *and* q_y *at* $U=4t$, $\beta=20/t$, $n=0.85$ *as obtained from parquet DΓA with an* 8×8 *cluster. Left-middle: Eigenvector* $v_{d_{x^2-y^2}}(\mathbf{k},\nu=\pi/\beta)$ *corresponding to the dominant eigenvalue in the particle-particle channel. Right-middle: Projection of* $v_{d_{x^2-y^2}}(\mathbf{k},\nu=\pi/\beta)$ *onto the Fermi surface as obtained by multiplying with* $|G|^2$ *at the lowest Matsubara frequency. Right: Eigenvector* $v_{d_{x^2-y^2}}(\mathbf{r},\nu=\pi/\beta)$ *Fourier-transformed to lattice space (in units of lattice vector* $a=1$*). From [66].*

superconducting eigenvector in real space, showing that the eigenvector describes a nearest-neighbor plus-minus structure, i.e., $d_{x^2-y^2}$, alternation.

Fig. 15 shows the same kind of analysis but now deeply in the overdoped regime, i.e., for $n=0.72$. Here, the magnetic susceptibility is peaked at an incommensurate wave vector $\mathbf{Q}_1=(\pi+\delta,\pi)$ [and symmetrically related $\mathbf{Q}_2=(\pi,\pi+\delta)$ etc.] similar as in Fig. 5 for the $3d$ Hubbard model. For the finite momentum clusters of parquet DΓA, δ can, as a matter of course, only take values congruent with the momentum grid. In this incommensurate case, the leading superconducting eigenvalue is not d-wave anymore but a higher-order $\bar{s}$-wave.

Fig. 15 (left-middle) shows the momentum dependence of this $\bar{s}$-wave, which becomes more obvious if we project onto the Fermi surface (right-middle). Because of the incommensurability, $\mathbf{Q}_1$ does not link the antinodal points $(0,\pm\pi)$ and $(\pm\pi,0)$ any longer as for $n=0.85$ in Fig. 14. Instead $\mathbf{Q}_1$ and $\mathbf{Q}_2$ connect the points of the Fermi surface which are close to the antinodal points $(0,\pm\pi)$ and $(\pm\pi,0)$ and have a large negative component of the eigenvector $v_{\bar{s}}$ to points that are in-between the nodal and antinodal point on the Fermi surface and have a large positive component of the eigenvector $v_{\bar{s}}$, see the $\mathbf{Q}_1$ and $\mathbf{Q}_2$ arrows in Fig. 15. In other words, the incommensurate antiferromagnetic ordering is not compatible with d-wave superconductivity any longer, but requires an even more complex $\mathbf{k}$-dependence of the order parameter (eigenvector for $\lambda=1$). This complex $\mathbf{k}$-dependence is dominated by terms $\cos(nk_x)\cos(nk_y)$ with $n=3,4$.

Fig. 15 (right) shows the eigenvector contributions in real space. This Figure makes clear why we call it an s-wave: all neighbors of the same shell of neighbors contribute with the same sign. In contrast, in Fig. 14 we have an alternating (d-wave) sign. Further, in Fig. 15 (right) it is not a next-nearest or local s-wave component that dominates. Instead the leading contribution stems from a relative lattice vector further away along the diagonal [$\mathbf{R}=(n,n)$ with $n=3,4$ in Fig. 15 (right)]. Kauch *et al.* hence coin it higher-order $\bar{s}$-wave: If we expand the angular dependence of $v_{\bar{s}}$ in terms of s, d-wave etc. it is an angular s-wave[14]; but it is of higher order

[14]More precise (but less common) would be to call it a a_{1g}-wave because the eigenvector belongs to this irreducible representation of the square lattice symmetry; there is no continuous rotational symmetry as s-wave might suggest.

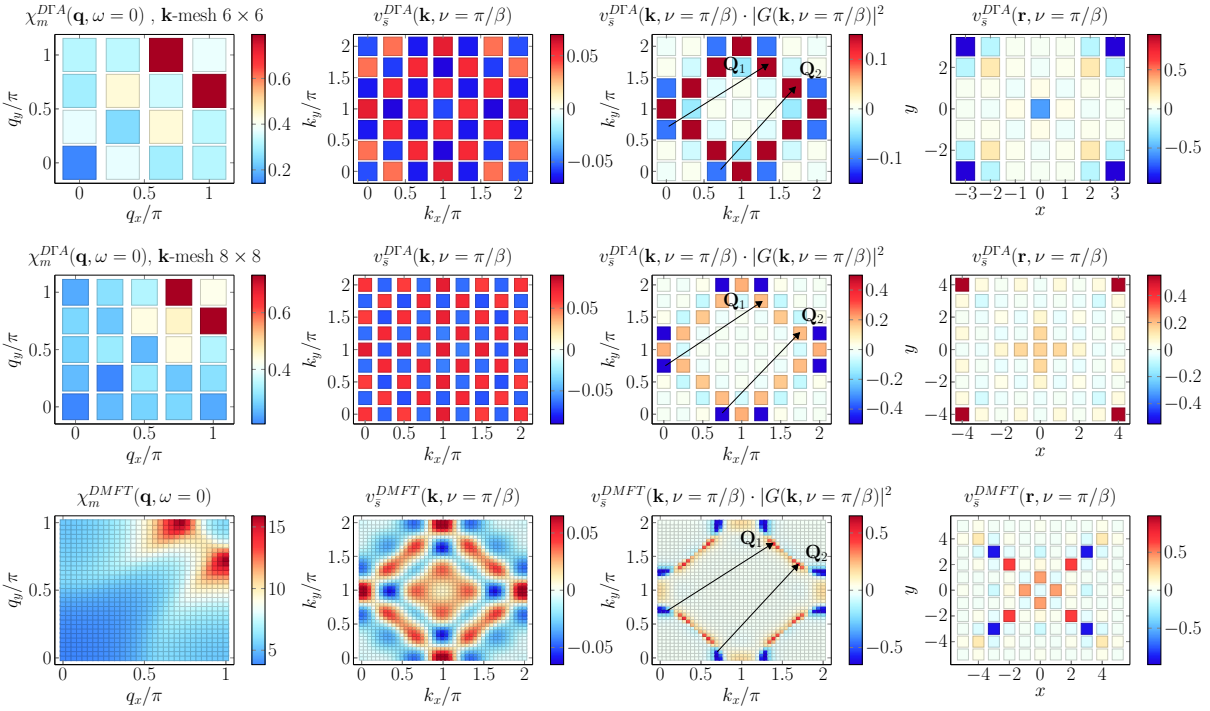

Fig. 15: *Parquet DΓA for a* 6×6 *(top) or* 8×8 *(middle) cluster, and simplified calculation on a larger cluster with DMFT susceptibility as a starting point (bottom). Left column: Magnetic susceptibility* $\chi_m(\mathbf{q}, \omega = 0)$ *vs.* q_x *and* q_y *at* $U = 5t$, $\beta = 15/t$, $n = 0.72$. *Left-middle column: Eigenvector* $v_{\bar{s}}(\mathbf{k}, \nu = \pi/\beta)$ *corresponding to the dominant eigenvalue in the particle-particle channel. Right-middle column: Projection of* $v_{\bar{s}}(\mathbf{k}, \nu = \pi/\beta)$ *onto the Fermi surface as obtained by multiplying with* $|G|^2$ *at the lowest Matsubara frequency. Right: Eigenvector* $v_{\bar{s}}(\mathbf{r}, \nu = \pi/\beta)$ *in real (lattice) space. From [66].*

in the radial expansion (couples further away neighbors). How far apart the coupled sites are depends on the specific incommensurable wave vector and is also influenced by the finite cluster size. But the auxiliary calculations, starting from the DMFT susceptibility on a large cluster [Fig. 15 (bottom)] further confirm that such a higher-order $\bar{s}$-wave phase naturally develops if the magnetic spin fluctuations are incommensurable.

7 Conclusion and outlook

To sum up, we have briefly recapitulated the DΓA method before reviewing recent highlights obtained with it: the calculation of critical exponents, quantum criticality, and superconductivity. In the following we will focus only on the latter two aspects. Quite generally, the advantage of diagrammatic extensions of DΓA is that they are able to describe short- and long-range correlations as well as temporal correlations, which become relevant at a quantum critical point. In Section 4, we have seen that particular lines on the Fermi surface of the $3d$ Hubbard model with nearest-neighbor hopping, so-called Kohn-lines, lead to a new universality class of critical exponents.

For studying a situation with $d + z < 4$, in Section 5 we turned to the periodic Anderson model in $d = 2$ at half-filling. This model describes a phase transition from an antiferromagnetic insulator to a Kondo insulator ($z = 1$). Here a quantum critical region could be identified, where the susceptibility shows a $\chi \sim T^{-2}$ behavior, whereas at higher temperatures $\chi \sim T^{-1}$. For a hybridization strength smaller than the QCP and for temperatures below the quantum critical region we eventually find an even stronger increase of χ. This is to be expected since even though there is no long-range antiferromagnetic order for $T > 0$ there is still an exponentially strong increase of the susceptibility and correlation length at low temperatures. For a hybridization strength larger than the QCP and for temperatures below the quantum critical region we are in the Kondo insulating regime so that eventually $\chi \to 0$ because of the (renormalized) single-particle excitation gap.
In Section 6 we turned to superconductivity in the $2d$ Hubbard model. We find d-wave superconductivity with a dome-like T_c-structure as a function of doping and a reasonable $T_c \approx 50\,\mathrm{K}$. Most interestingly, an order of magnitude larger T_c's, i.e., room temperature superconductivity, would be possible if the vertex would not be screened at low frequencies by particle-particle diagrams. Understanding this suppression of T_c gives us hope for identifying new routes towards higher T_c's. At large doping levels, we find a high-order $\bar{s}$-wave superconductivity to be the dominant superconducting channel, which is a natural consequence of having incommensurate antiferromagnetic spin fluctuations.
Up to now, the focus of diagrammatic extensions of DMFT has been on method development and applications to simple models such as the Hubbard, the periodic Anderson, and Falicov Kimball model. As a first step such model calculations are crucial for better understanding physics. In the future we will see many more applications to non-equilibrium and real materials. First realistic materials calculations [67] have already been performed for $SrVO_3$ using *ab initio* DΓA [67]. This AbinitoDΓA (`ADGA`) code for solving multi-orbital ladder DΓA equations including non-local interactions is made available via Gnu Public license [68]. For the model Hamiltonians studied in these lecture notes, instead, the one-orbital ladder DΓA code (`ladderDGA` [69]) with Moriyaesque λ correction and the `victory` code [70] for solving the parquet equations have been used.

Acknowledgments

First of all, I would like to thank my close and in many cases long-term co-workers in the research area of diagrammatic extensions of DMFT: A. Galler, P. Gunacker, A. Kauch, J. Kaufmann, A. Katanin, M. Kitatani, G. Li, P. Pudleiner, T. Ribic, G. Rohringer, G. Sangiovanni, T. Schäfer, C. Taranto, P. Thunström, J. Tomczak, A. Toschi, A. Valli, and M. Wallerberger. Without them, the development presented in these Lecture Notes would not have been possible. Secondly I acknowledge financially support by the European Research Council under the European Union's Seventh Framework Program (FP/2007-2013) through ERC Grant No. 306447, and the Austrian Science Fund (FWF) through project P30997.

References

[1] W. Metzner and D. Vollhardt, Phys. Rev. Lett. **62**, 324 (1989)

[2] A. Georges and G. Kotliar, Phys. Rev. B **45**, 6479 (1992)

[3] A. Georges, G. Kotliar, W. Krauth, and M.J. Rozenberg, Rev. Mod. Phys. **68**, 13 (1996)

[4] K. Held, I.A. Nekrasov, G. Keller, V. Eyert, N. Blümer, A.K. McMahan, R.T. Scalettar, T. Pruschke, V.I. Anisimov, and D. Vollhardt, Phys. Status Solidi B **243**, 2599 (2006), previously appeared as Psi-k Newsletter No. 56 (April 2003)

[5] G. Kotliar, S.Y. Savrasov, K. Haule, V.S. Oudovenko, O. Parcollet, and C.A. Marianetti, Rev. Mod. Phys. **78**, 865 (2006)

[6] K. Held, Adv. Phys. **56**, 829 (2007)

[7] T.A. Maier, M. Jarrell, T.C. Schulthess, P.R.C. Kent, and J.B. White, Phys. Rev. Lett. **95**, 237001 (2005)

[8] A. Toschi, A.A. Katanin, and K. Held, Phys. Rev. B **75**, 045118 (2007)

[9] A.N. Rubtsov, M.I. Katsnelson, and A.I. Lichtenstein, Phys. Rev. B **77**, 033101 (2008)

[10] G. Rohringer, A. Toschi, H. Hafermann, K. Held, V.I. Anisimov, and A.A. Katanin, Phys. Rev. B **88**, 115112 (2013)

[11] C. Taranto, S. Andergassen, J. Bauer, K. Held, A. Katanin, W. Metzner, G. Rohringer, and A. Toschi, Phys. Rev. Lett. **112**, 196402 (2014)

[12] T. Ayral and O. Parcollet, Phys. Rev. B **92**, 115109 (2015)

[13] G. Li, Phys. Rev. B **91**, 165134 (2015)

[14] G. Rohringer, H. Hafermann, A. Toschi, A.A. Katanin, A.E. Antipov, M.I. Katsnelson, A.I. Lichtenstein, A.N. Rubtsov, and K. Held, Rev. Mod. Phys. **90**, 025003 (2018)

[15] G. Rohringer, A. Toschi, A. Katanin, and K. Held, Phys. Rev. Lett. **107**, 256402 (2011)

[16] D. Hirschmeier, H. Hafermann, E. Gull, A.I. Lichtenstein, and A.E. Antipov, Phys. Rev. B **92**, 144409 (2015)

[17] A.E. Antipov, E. Gull, and S. Kirchner, Phys. Rev. Lett. **112**, 226401 (2014)

[18] T. Schäfer, A.A. Katanin, K. Held, and A. Toschi, Phys. Rev. Lett. **119**, 046402 (2017)

[19] T. Schäfer, M. Kitatani, A.A. Katanin, A. Toschi, and K. Held, (unpublished) (2018)

[20] A.A. Katanin, A. Toschi, and K. Held, Phys. Rev. B **80**, 075104 (2009)

[21] J. Otsuki, H. Hafermann, and A.I. Lichtenstein, Phys. Rev. B **90**, 235132 (2014)

[22] T. Schäfer, F. Geles, D. Rost, G. Rohringer, E. Arrigoni, K. Held, N. Blümer, M. Aichhorn, and A. Toschi, Phys. Rev. B **91**, 125109 (2015)

[23] A.N. Rubtsov, M.I. Katsnelson, A.I. Lichtenstein, and A. Georges, Phys. Rev. B **79**, 045133 (2009)

[24] C. Jung: *Superperturbation theory for correlated fermions*, Ph.D. thesis, University of Hamburg, 2010

[25] T. Schäfer, A. Toschi, and K. Held, J. Magn. Magn. Mater. **400**, 107 (2016)

[26] M. Kitatani, N. Tsuji, and H. Aoki, Phys. Rev. B **92**, 085104 (2015)

[27] K. Held: *Dynamical Vertex Approximation* in E. Pavarini, E. Koch, D. Vollhardt, A.I. Lichtenstein (eds.): *Autumn School on Correlated Electrons. DMFT at 25: Infinite Dimensions* Modeling and Simulation, Vol. 4 (Forschungszentrum Jülich, 2014) [arXiv:1411.5191]

[28] C. De Dominicis, J. Math. Phys. **3**, 983 (1962)

[29] C. De Dominicis and P.C. Martin, J. Math. Phys. **5**, 14 (1964)

[30] N.E. Bickers: *Theoretical Methods for Strongly Correlated Electrons* (Springer-Verlag New York Berlin Heidelberg, 2004), Ch. 6, pp. 237–296

[31] T. Ribic, P. Gunacker, S. Iskakov, M. Wallerberger, G. Rohringer, A.N. Rubtsov, E. Gull, and K. Held, Phys. Rev. B **96**, 235127 (2017)

[32] E. Gull, A.J. Millis, A.I. Lichtenstein, A.N. Rubtsov, M. Troyer, and P. Werner, Rev. Mod. Phys. **83**, 349 (2011)

[33] P. Gunacker, M. Wallerberger, E. Gull, A. Hausoel, G. Sangiovanni, and K. Held, Phys. Rev. B **92**, 155102 (2015)

[34] P. Gunacker, M. Wallerberger, T. Ribic, A. Hausoel, G. Sangiovanni, and K. Held, Phys. Rev. B **94**, 125153 (2016)

[35] G. Rohringer, A. Valli, and A. Toschi, Phys. Rev. B **86**, 125114 (2012)

[36] G. Rohringer and A. Toschi, Phys. Rev. B **94**, 125144 (2016)

[37] L.S. Ornstein and F. Zernike, Proc. Roy. Acad. Amsterdam **17**, 793 (1916)

[38] C. Holm and W. Janke, Phys. Rev. B **48**, 936 (1993)

[39] M.E. Fisher, Rep. Prog. Phys. **30**, 615 (1967)

[40] P. Sémon and A.-M.S. Tremblay, Phys. Rev. B **85**, 201101 (2012)

[41] N. Goldenfeld: *Lectures On Phase Transition And The Renormalization Group* (CRC Press, 2018)

[42] L. Del Re, M. Capone, and A. Toschi, arxiv:1805.05194 (2018)

[43] H. v. Löhneysen, A. Rosch, M. Vojta, and P. Wölfle, Rev. Mod. Phys. **79**, 1015 (2007)

[44] J.A. Hertz, Phys. Rev. B **14**, 1165 (1976)

[45] A.J. Millis, Phys. Rev. B **48**, 7183 (1993)

[46] T. Moriya: *Spin Fluctuations in Itinerant Electron Magnetism* (Springer Verlag, Berlin, Heidelberg, 1985)

[47] J.-X. Zhu, D.R. Grempel, and Q. Si, Phys. Rev. Lett. **91**, 156404 (2003)

[48] Q. Si and J.L. Smith, Phys. Rev. Lett. **77**, 3391 (1996)

[49] R. Chitra and G. Kotliar, Phys. Rev. Lett. **84**, 3678 (2000)

[50] W. Kohn, Phys. Rev. Lett. **2**, 393 (1959)

[51] A. Hewson: *The Kondo Problem to Heavy Fermions* (Cambridge University Press, 1993)

[52] T. Pruschke, R. Bulla, and M. Jarrell, Phys. Rev. B **61**, 12799 (2000)

[53] S. Doniach, Physica B+C **91**, 231 (1977)

[54] J. Otsuki, H. Kusunose, and Y. Kuramoto, Phys. Rev. Lett. **102**, 017202 (2009)

[55] N.D. Mermin and H. Wagner, Phys. Rev. Lett. **17**, 1307 (1966)

[56] S. Chakravarty, B.I. Halperin, and D.R. Nelson, Phys. Rev. Lett. **60**, 1057 (1988)

[57] A.V. Chubukov, S. Sachdev, and J. Ye, Phys. Rev. B **49**, 11919 (1994)

[58] M. Troyer, M. Imada, and K. Ueda, J. Phys. Soc. Jpn **66**, 2957 (1997)

[59] D.J. Scalapino, Rev. Mod. Phys. **84**, 1383 (2012)

[60] M. Kitatani, T. Schäfer, H. Aoki, and K. Held, arXiv:1801.05991 (2018)

[61] B. Kyung, J.-S. Landry, and A.-M.S. Tremblay, Phys. Rev. B **68**, 174502 (2003)

[62] T. Maier, M. Jarrell, T. Pruschke, and M.H. Hettler, Rev. Mod. Phys. **77**, 1027 (2005)

[63] J. Vučičević, T. Ayral, and O. Parcollet, Phys. Rev. B **96**, 104504 (2017)

[64] H. Hafermann, M. Kecker, S. Brener, A.N. Rubtsov, M.I. Katsnelson, and A.I. Lichtenstein, J. Supercond. Nov. Magn. **22**, 45 (2009)

[65] W. Metzner, M. Salmhofer, C. Honerkamp, V. Meden, and K. Schönhammer, Rev. Mod. Phys. **84**, 299 (2012)

[66] A. Kauch, F. Hörbinger, G. Li, and K. Held, (unpublished) (2018)

[67] A. Galler, P. Thunström, P. Gunacker, J.M. Tomczak, and K. Held, Phys. Rev. B **95**, 115107 (2017)

[68] A. Galler, P. Thunström, J. Kaufmann, M. Pickem, J.M. Tomczak, and K. Held, arXiv:1710.06651 (2017)

[69] G. Rohringer, A. Katanin, T. Schäfer, A. Hausoel, K. Held, and A. Toschi, github.com/ladderDGA (2018)

[70] G. Li, A. Kauch, P. Pudleiner, and K. Held, arXiv:1708.07457 (2017)